Journal of Microscopy

Journal of Microscopy, 2013
Received 14 November 2012; accepted 14 March 2013

doi: 10.1111/jmi.12039

Nanoscale characterization of gold nanoparticles created by *in situ* reduction at a polymeric surface

A. DUTTA*,†, C.J. CLUKAY‡, C.N. GRABILL‡, D.J. FREPPON‡, A. BHATTACHARYA*, S.M. KUEBLER‡,§ & H. HEINRICH*,†

*Department of Physics, University of Central Florida, Orlando, Florida, U.S.A.

†Advanced Materials Processing and Analysis Center, University of Central Florida, Orlando, Florida, U.S.A.

‡Department of Chemistry, University of Central Florida, Orlando, Florida, U.S.A.

§CREOL, The College of Optics and Photonics, University of Central Florida, Orlando, Florida, U.S.A.

Key words. Gold, HAADF-STEM, nanoparticles, polymer, SU-8, TEM.

Summary

Transmission Electron Microscopy is used as a quantitative method to measure the shapes, sizes and volumes of gold nanoparticles created at a polymeric surface by three different *in situ* synthesis methods. The atomic number contrast (*Z*-contrast) imaging technique reveals nanoparticles which are formed on the surface of the polymer. However, with certain reducing agents, the gold nanoparticles are additionally found up to 20 nm below the polymer surface. In addition, plan-view high-angle annular dark-field scanning transmission electron microscopy images were statistically analyzed on one sample to measure the volume, height and effective diameter of the gold nanoparticles and their size distributions. Depth analysis from high-angle annular dark-field scanning transmission electron microscopy micrographs also gives information on the dominant shape of the nanoparticles.

Introduction

Electroless deposition of metals onto nonconductive surfaces is a widely used process in electronics (e.g. metallizing printed wiring boards, magnetic recording), silvering of mirrors and decorative arts (Mallory & Hajdu, 1990). New applications are possible in the optical field for electroless silver deposition of three-dimensional metamaterials (Yan *et al.*, 2011). In electroless deposition, a reducing agent transfers electrons to metal ions at a catalytic surface of a material, while the rate of metal cluster formation within the solution is slower than at the surface. For electroless deposition of nanoparticles (NPs) and layers on nonconductive surfaces, the composition of the solution, temperature, stirring speed and pH value determine the speed of the deposition process (Taleb *et al.*, 2011). However, other parameters, such as the sample surface, can also influence the deposition process. Gold nanoparticles (Au NPs) have been used as nucleation sites for silver deposition (Knake *et al.*, 2005; Taleb *et al.*, 2011), and we study here the arrangement, size and depth of Au NPs on a surface and their influence on the deposition of silver NPs on the surface.

In this paper, we study initial Au NPs deposited by different methods onto films of the cross-linkable epoxide SU-8 (Campo & Greiner, 2007). The goal of the work presented here is to understand the correlation between processing and the Au NP distribution and size on the polymer surface. We also suggest a fast way for the quantitative analysis of Au NPs prepared by depositing Au NPs on SU-8 polymer surface by sodium borohydride ($NaBH_4$) reduction.

Sample preparation

Polymer cross-linking and reduction by $NaBH_4$

Square 25 mm × 25 mm glass substrates were cleaned by immersion in aqueous 1.0 M KOH (Fisher, Hampton, NH, U.S.A.) (CAS# 1310-58-3) for 1 h, rinsing with copious deionized water, and drying in the oven (at 100°C). Cross-linked SU--8 films were prepared by spin coating SU-8 2035 resin (MicroChem, Newton, MA, U.S.A.) onto cleaned substrates. Substrates were cured by baking to remove the solvent at 65°C for 3 min followed by 95°C for 6 min. The substrates where then irradiated for 3 min using a broadband UV source (Loctite, Germany) (ZETA 7411-5, 400 W metal halide source, 315–400 nm) with a longpass filter PL-360LP (Omega Optical, Brattleboro, VT, U.S.A.), cut-off 360 nm, before baking exposures for 60 s at 65°C, 15 min at 95°C and 60 s at 65°C. The cross-linked polymeric films

Correspondence to: Helge Heinrich, CREOL, Department of Physics, University of Central Florida, Orlando, FL 32816, U.S.A. Tel: +1-407-823-1884; fax: +1-407-882-1502; e-mail: helge.heinrich@ucf.edu

were functionalized with ethylene diamine (Chen *et al.*, 2007), tetraethylenepentamine or *N*-aminoethylenepeparazine. Functionalization with ethylene diamine was achieved by immersing the cross-linked polymer film into a 20% 1, 2-diaminoethane (Acros, Belgium) (CAS# 107-15-3) in ethanol for 60 min, rinsing with copious ethanol, then water, then allowing to dry by standing in air.

The amine functionalized polymeric samples were treated with an aqueous solution of 5.3×10^{-4} M $HAuCl_4$ (Acros, Hampton, NH, U.S.A.) (CAS# 16961-25-4) for 30 min, rinsed with copious deionized water. For reduction, the samples were immersed in 0.1 M aqueous $NaBH_4$ (Fisher, Hampton, NH, U.S.A) (CAS# 16940-66-2) for 60 s, rinsed with copious deionized water, and allowed to dry by standing in air (DiScipio, 1996; Daniel & Astruc, 2004; Khalid *et al.*, 2009). Reduction using citrate was accomplished by immersing samples for 8 h in aqueous 1% (w/v) sodium citrate ($Na_3C_6H_5O_7$, Fisher, CAS# 6132-04-3) (Khalid *et al.*, 2009). Reduction with hydroquinone was achieved by immersing samples in aqueous 0.1 M hydroquinone (Acros, HOC_6H_4OH, CAS# 123-31-9) for 1 h (Danscher, 1981). After reduction, samples were rinsed with copious water and allowed to dry by standing in air.

Sample preparation for transmission electron microscopy (TEM)

To increase contrast of cross-sectional images in TEM the Au-deposited samples were first coated with carbon for 30 s in a vacuum evaporator (Jeol JEE 4X, Japan). To improve conductivity and contrast in the Focused Ion Beam (FIB), the C-coated samples were coated with an Au-Pd alloy for 3–4 min in a sputter coater (Emitech K550, UK) which uses a 60 mm diameter and 0.1 mm thick magnetron target assembly giving fine grains without the need to cool the specimen.

An FIB (FEI, Hillsboro, OR, U.S.A.) system operating at 30 kV was used to prepare cross-sectional TEM samples of the Au samples. The FIB system can be operated at low-beam currents for imaging or high-beam currents for site-specific sputtering or milling and can reach a lateral resolution of 5 nm. A 1-μm thick platinum layer was deposited on the sample surface on a typical rectangular area of 20 μm (length) $\times$ 1 μm (width) to protect the interior of the FIB cross section from gallium ion implantation with the help of the Pt deposition system within the instrument. Milling is carried out on the desired rectangular area with precise control by using smaller ion beam sizes with lower currents in the final steps (Anderson, 2002; Loos *et al.*, 2002; Li *et al.*, 2006; Brostow *et al.*, 2007). Currents as low as 50 pA were used for the final thinning of the sample to prevent back deposition of gallium ions and to limit the thickness of the amorphous (radiation damaged) layer forming at the surfaces of the FIB cross section (Patterson *et al.*, 2002; Huang, 2004). The typical dimensions of the final sample were 16 μm (length) $\times$ 4 μm (height) $\times$ 50 nm (thickness). A Mitutoyo (Japan) VM Zoom 40 optical microscope equipped with hydraulic micromanipulators was used for *ex situ* lift out from the bulk and for placement of the TEM sample on a holey carbon-coated Cu grid (McMahon *et al.*, 2009). The FIB technique of preparing cross sections was not used to produce the plan-view samples. Instead, a portion of the Au-deposited film on the glass substrate was scraped off with tweezers and placed directly on the Cu TEM grid.

Experiments

High-resolution TEM

The samples were studied in a TECNAI F30 TEM (FEI, Hillsboro, OR, U.S.A.) equipped with a field emission source operating at 300 kV with a point to point resolution of 0.2 nm and a maximum allowable specimen tilt of $\pm 40^\circ$. Both lower magnification and high-resolution images were acquired. In the scanning transmission electron microscopy (STEM) mode, a Fischione high-angle annular dark-field (HAADF) detector with a contrast/brightness setting of 12.5% and 46.875% and a camera length of 80 mm was consistently used (Yuan *et al.*, 2010). This setting allowed for a quantitative calibration of the contrast of the Au NPs. Energy dispersive spectroscopy and energy-filtered TEM were employed for compositional analysis.

HAADF-STEM

The HAADF technique has the advantage that the contrast is highly dependent on the atomic number of the material and not on the crystal orientation; it provides structural and chemical information with atomic resolution (Nellist & Pennycook, 1998; James & Browning, 1999). The quantitative measurement of the thickness and volume of Au NPs from images of plan-view samples requires the intensity calibration of the HAADF detector intensity. To accomplish the contrast calibration, the HAADF detector intensity was measured in the direct imaging mode and the corresponding charge-coupled device (CCD) camera intensity was recorded in the diffraction mode. The beam intensities were measured for different spot sizes, gun lenses and condenser aperture sizes keeping the extraction voltage in the electron microscope constant. The HAADF detector shows some variability (about 10%) of its sensitivity depending on where the electron beam hits the detector. The insert in Figure 1 shows an image of the HAADF detector. The background signal in the dark areas of the insert shows variations of less than 3% and a linear interpolation of the background signal over the bright detector area was used. The background was subtracted and the intensities were averaged ($I_{HAADF,avg}$) over the HAADF detector for calibration of different incident electron beam probes (Fig. 1). We found that the HAADF detector intensity scales with the linear CCD signal and can be best fitted as the following:

$$I_{HAADF,avg} = AI_{CCD}^{B}, \quad (1)$$

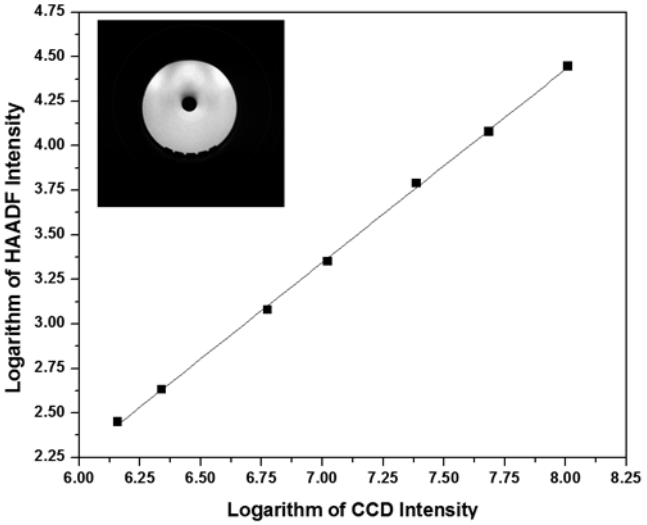

Fig. 1. Plot of the intensity of the HAADF detector versus CCD camera intensity for HAADF detector calibration.

where $I_{HAADF,avg}$ is the intensity of the HAADF detector, I_{CCD} is the intensity (per second) of the CCD detector, A and B are constants (Kübel *et al.*, 2005).

$$\log I_{HAADF,avg} = B \log I_{CCD} + \log A.$$

The following values were found: slope $B = 1.098\ (\pm 0.016)$, $A = (4.48 \pm 0.14)^{*}10^{-5}$ and the correlation coefficient $R = 0.99981$.

$$I_{HAADF,avg} = (4.48 \pm 0.14)^{*}10^{-5} I_{CCD}^{1.098(\pm 0.016)}. \qquad (2)$$

After the calibration of the detector signal to correctly account for nonlinear effects, the fraction of electrons scattered onto the HAADF detector for each scan position in an experiment is obtained. Before and after the HAADF-STEM measurement for an Au sample, a STEM image of the detector (in imaging mode) is acquired. This measurement is done twice to ensure that the electron beam intensity did not change during the acquisition of HAADF-STEM images. Au NPs of diameter 50–60 nm were used to find the fraction of scattered electrons per nm of the Au sample. Among the NPs viewed without sample tilt and two sample tilts of 45° and -42°, several showed no change in diameter indicating a nearly spherical shape. In addition, the measured HAADF-STEM intensity of those selected NPs did not change significantly for the three viewing directions. The measured diameter (49.5 ± 0.2 nm) and the corresponding volume ($V = 6.34 \times 10^4$ nm^3) of the selected NP shown in Figure 2 remains the same when the sample is tilted in the microscope holder in the positive and negative direction thus confirming its spherical shape. In addition to HAADF-STEM micrographs, bright field–TEM images of the same NPs were taken to confirm the measured diameters and shapes at the three sample tilt angles.

Summation of the intensities of each pixel ($\sum I$) over the whole NP gives us $(\frac{\sum I}{I\,HAADF,avg})^{*}(\frac{pixel\ area^2}{V}) = 0.213\%$, representing the fraction of the HAADF signal intensity per nm of Au thickness relative to the HAADF intensity for the incident beam directly on the detector. Taking the average of several Au NP measurements, this signal fraction is $0.207 \pm 0.010\%$. After correcting for the nonlinearity of the HAADF detector, the fraction of scattered electrons is 0.25% per nm of Au thickness with the above detector brightness and contrast settings. The local thickness of the selected NP shown in Figure 2 is determined from the HAADF intensity of a cross section through the NPs' centre. This measured local thickness corresponds well to the local thickness assuming a spherical particle as shown in Figure 3.

Results and discussion

Morphology of Au NPs from bright field imaging

Direct evidence concerning the morphology, size and density comes from the TEM studies of colloidal Au bound to SU-8 polymer on the TEM grids. Figures 4(a), (b) and (c) show the bright field–TEM micrograph of Au NPs formed on SU-8 polymer using three different reducing agents of varying standard reduction potential.

TEM images reveal crystalline NPs with typical {111} and {200} lattice plane spacing. For hydroquinone-reduced Au, the Au NPs form a band on or near the surface of the polymer,

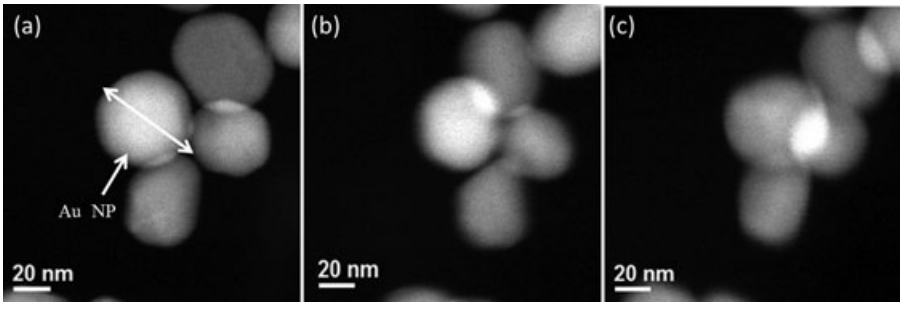

Fig. 2. (a–c) STEM micrographs of Au NPs 50–60 nm in diameter at 0°, 45° and -42° tilt of the TEM holder. The tilt axis is vertical and the particle diameter along a line across the nanoparticle marked in (a) remained constant.

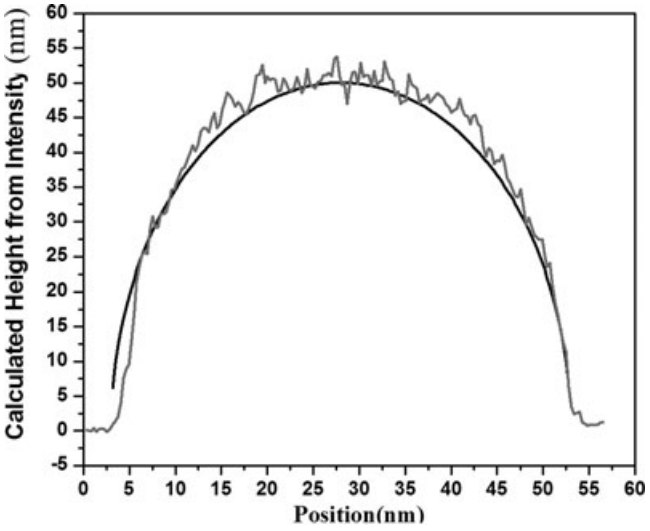

Fig. 3. Height of the selected nanoparticle in Figure 2 from HAADF Intensity (solid grey line) and from local thickness (solid black line).

with particle sizes in the 5—10 nm range, as shown in Figure 4(a). As hydroquinone is a bulky reducing agent, there is less penetration into the polymer matrix, so the NPs are mostly formed near the surface of the polymer confirming recent findings by Taleb *et al.* (2011). Figure 4(b) shows Au NPs that are 10–15 nm in diameter formed by citrate reduction of Au^{3+} ions. These Au NPs formed by citrate reduction are found on the surface as well as up to 20 nm below the surface of the polymer. Smaller NPs of 3–4 nm average diameter are formed 20 nm inside the polymer matrix, whereas larger Au NPs of 12–15 nm average diameter are found only on the surface. Au NPs are formed on or near the surface of the polymer by reduction of Au ions by $NaBH_4$ as can be seen in Figure 4(c). The NPs are spherical in shape and they are of range 2–5 nm in diameter with almost no faceting. Moreover, the Au NPs are aligned along a straight line 10–20 nm below the polymer surface. $NaBH_4$ is a strong reducing agent which produces small Au NPs whereas hydroquinone, having a higher standard reduction potential, generates bigger NPs. Moreover, hydroquinone, being a bulky molecule, fails to penetrate the polymer matrix to act upon the Au^{3+} ions that have adsorbed into the polymer matrix. Bright-field TEM images in Figures 4(a) and (b) suggest that when hydroquinone acts as reducing agent the Au NPs have smaller height (4–5 nm in diameter) than when formed by sodium citrate, in which case they are 10–15 nm in height. The measurement of the height confirms that the NPs are spherical in shape and they are not faceted.

Quantitative analysis of HAADF-STEM images

Plan-view samples were studied in the STEM mode using the HAADF detector. Evaluation of the NP size, volume and

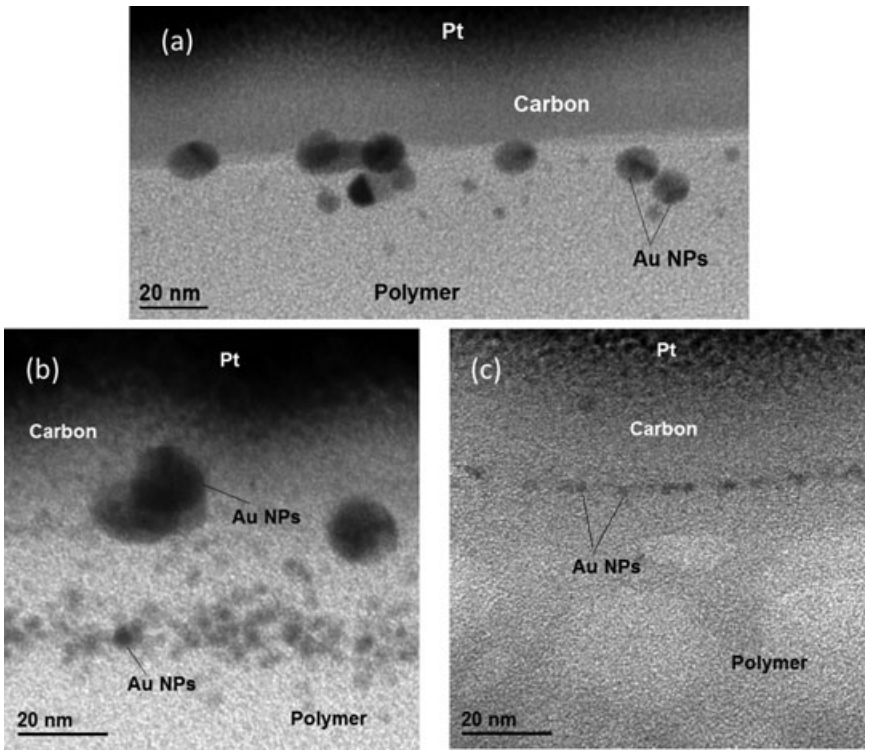

Fig. 4. (a) Cross-sectional Bright Field (BF) TEM micrographs of Au NPs formed by reduction with hydroquinone (HQ). (b) Au NPs formed from reduction of Au^{3+} ions by sodium citrate. (c) $NaBH_4$ reduced Au NPs on the SU-8 polymer surface.

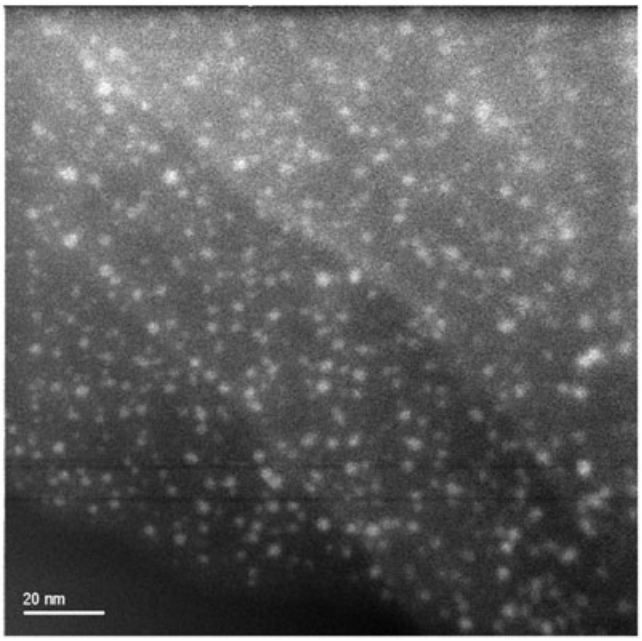

Fig. 5. Plan-view HAADF STEM image of Au NPs formed from reduction by $NaBH_4$ deposited on SU-8 polymer.

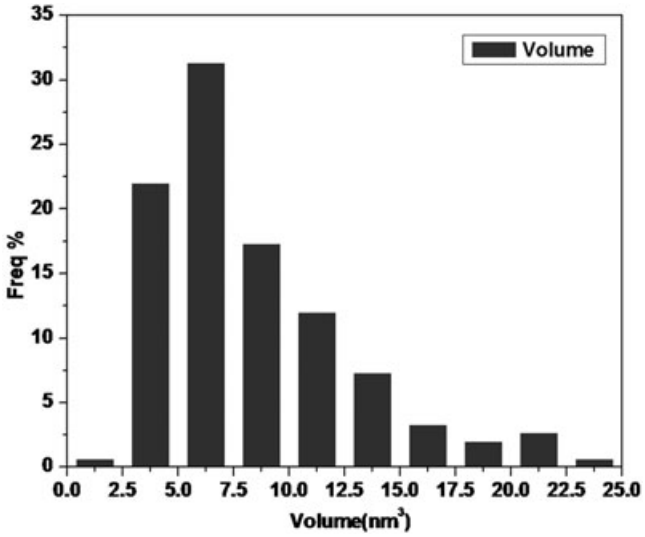

Fig. 6. Volume distribution of 150 Au NPs.

distribution on the surface has been carried out in the past using HAADF images (Prestridge *et al.*, 1977; Sanders, 1986; Menard *et al.*, 2006a, 2006b; Heinrich *et al.*, 2009). A representative plan-view HAADF-STEM image of an Au deposited sample from reduction by $NaBH_4$ is shown in Figure 5. The Au NPs, which can be seen as bright contrast features on the dark contrast SU-8 polymer, can be thought of as isolated particles deposited on the SU-8 polymer. An integration time of 10 μs for each of the 2048 $\times$ 2048 pixels was used to acquire the HAADF-STEM images. In the STEM mode with a HAADF detector, atomic number contrast was used to identify the NPs and to measure their sizes. The intensity-calibrated HAADF-STEM image confirms that the (1) the particles are isolated, evenly spaced and not aggregated in two dimensions; (2) the particle coverage is uniform over areas macroscopic compared to the particle size and (3) only about 25% of the surface is covered without much long-range ordering.

To obtain information about the heights of the NPs, quantification of the intensity distribution in the calibrated STEM image is necessary. For incoherent scattering conditions in HAADF, the final pixel intensity consists of the sum of the individual scattering contributions from Au atoms together with the background signal (Williams & Carter, 1996; Lockwood, 2007).

$$I_{Final} = I_{Au} + I_B, \tag{3}$$

where I_B is the background signal of the image, which can be easily determined considering that the thickness of the polymer layer is either constant or linearly changing over the area of each NP. Polymer layers without NPs were used to test how thickness changes affect the HAADF-STEM signal. The image intensity modulations caused by thickness variations of the polymer appear on a scale of significantly more than 20 nm. The amplitude variations of the signal due to the polymer are at most 20% of the intensity caused by Au NPs of 2 nm diameter. However, these small background intensity variations appear on a larger scale than the size of the NPs studied here. The background signal was therefore determined around each NP and a linear interpolation of this background signal was subtracted from the image intensities of each NP. A total of 150 NPs with observable intensity were manually evaluated from the images using the Digital Micrograph (Gatan Inc.) software package. The volume of each NP was determined from the sum of the intensities over the total number of pixels considering the size of each pixel. From the intensity calibration, the volume of each NP was determined. A mean thickness was obtained for each NP, as well as the volume. The corresponding volume distribution is shown in Figure 6.

It has to be noted that $NaBH_4$ is a strong reducing agent which produces small surface bound NPs (Reetz *et al.*, 2000; Troupis *et al.*, 2008; Shankar *et al.*, 2010). The average volume $<V>$ of the NPs was found to be 8 nm^3 with a 56% relative standard deviation whereas the average area $<A>$ of the NPs was determined to be 6.5 nm^2 with a particle size distribution width of 0.7 nm. Considering the Au NPs to be circular in cross section, the height of each NP was calculated from geometry and is given by

$$H_t = 1.5 \times Average\ Thickness. \tag{4}$$

The height distribution of the Au NPs is shown in Figure 7. The NP height distribution shows that almost 60% of the particles have a height of (1–2) nm. A positive skewness

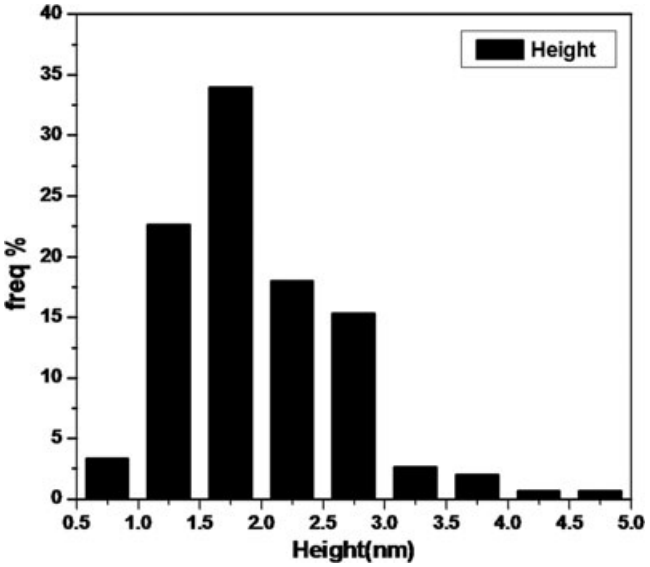

Fig. 7. Height distribution of Au NPs from calibrated HAADF-STEM micrographs.

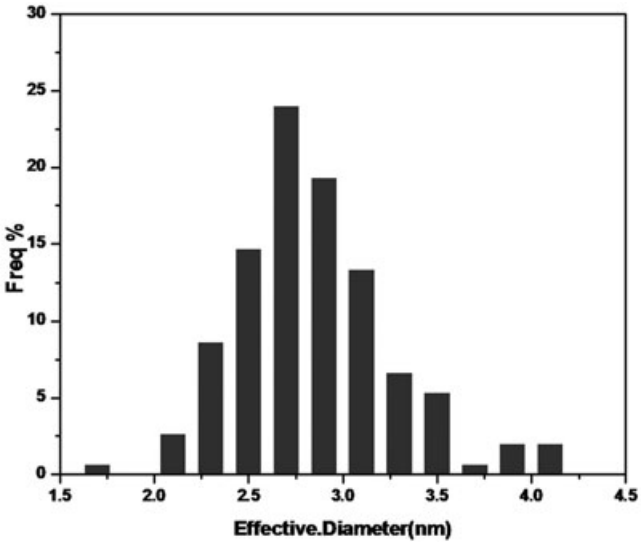

Fig. 8. Distribution of the effective diameter of Au NPs.

value depicts the asymmetry of the distribution and that most NPs have heights below the average height of all the NPs.

The average Au NP height ($<H_t>$) is calculated taking into consideration the nonlinearity of the HAADF detector. The NPs were considered to be circular in cross section and yield a value for $<H_t>$ of 1.97 nm for the 150 NPs. The standard deviation of the height of the NPs σ_H was found to be 0.74 nm from the measurements.

A further attempt was made to study the detailed morphology of the Au NPs if we consider the NPs as ellipsoidal. The in-plane projected shape of the NPs is found to be elliptic rather than circular with a long axis x_n and a short axis y_n, giving an effective diameter of $D_n = \sqrt{x_n y_n}$. Independent of the first measurements where we assumed a circular projection, the long and the short diameter were now measured manually for each NP. The same NPs were analyzed again to determine the shape and size (volume) of each NP. This independent measurement of NP volumes was also performed to test if the criteria for background subtraction and determination of cross-sectional area can be consistently applied.

The effective diameter of the particles distribution is shown in Figure 8. The average effective diameter D_n of Au NPs is 2.84 nm with a majority of NPs having a diameter between 2.5 and 3 nm. The in-plane aspect ratio $\left(\frac{y_n}{x_n}\right)$ of less than 1 suggests that most of the Au NPs are oblate spheroids with $<(\frac{y_n}{x_n})>$ of 0.90. Only about 5% of the measured NPs show no deviation from circular projected shape. Further considering that the NPs are ellipsoids having height H_n, the volume is given by $V_n = \frac{\pi x_n y_n H_n}{6}$. The in-plane and out-of-plane aspect ratio $(\frac{y_n}{x_n})$ and $(\frac{H_n}{D_n})$ are shown in the histograms of Figures 9 and 10. After measuring and evaluating the sizes of 150 NPs, the dimensions of each NP were determined

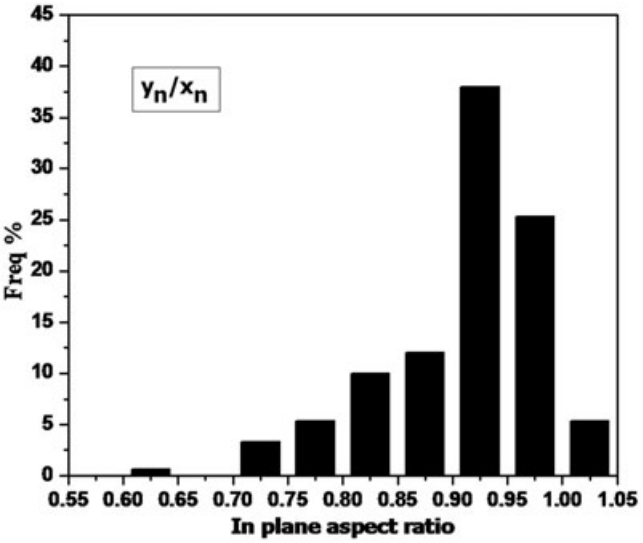

Fig. 9. In-plane aspect ratio of Au NPs distribution.

again in a separate measurement. This was done to check if the data evaluation from the HAADF-STEM micrographs was consistent.

The mean out of plane aspect ratios $<\frac{H_n}{D_n}>$ for both independent measurements (the first measurement is indexed as '$n1$' and the second as '$n2$' in the following) are 0.64 and 0.66, respectively. The mean value $<H>$ and standard deviation σ_H of the height distribution are smaller than the corresponding $<D_n>$ and σ_D values which prove the assumption that the NPs are ellipsoids.

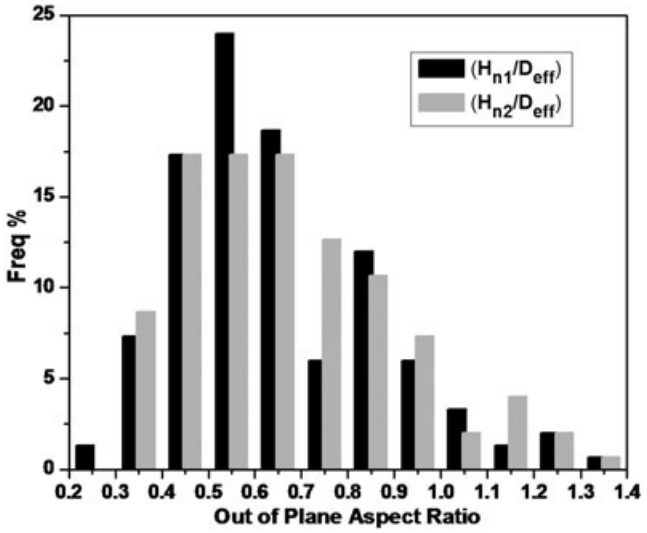

Fig. 10. Out of plane aspect ratio of Au NPs distribution.

The standard deviation in the height and volume of the NPs is given by

$$\sigma_H = \sqrt{\frac{\sum(H_{n1} + H_{n2} - 2 <H>^2)}{4N}} \;\; \& \;\; \sigma_V = \sqrt{\frac{\sum(V_{n1} + V_{n2} - 2 <V>^2)}{4N}}, \tag{5}$$

whereas the error in the HAADF-STEM data evaluation is

$$\varepsilon_H = \sqrt{\frac{\sum(H_{n1} + H_{n2})^2}{N}} \;\; \& \;\; \varepsilon_V = \sqrt{\frac{\sum(V_{n1} + V_{n2})^2}{N}}, \tag{6}$$

where N is the total number of NPs, V_{n1} and V_{n2} are the volumes from calibrated HAADF-STEM images from the two separate measurements. Calculated ε_H and ε_V values from Eq. (5) are 0.04 nm and 1.48 nm^3. ε_H is much smaller than σ_H, i.e. the measurement error in the height measurement is significantly smaller than the standard deviation in the size distribution.

Conclusions

This work presents data from the direct measurement of volumes of Au NPs using TEM. While several research papers (LeBeau *et al.*, 2008a,b, 2009; Aert *et al.*, 2009) have provided quantitative thickness and compositional data using the HAADF-STEM measurements, the above methods and analyses provide high accuracy in the determination of particle size distributions as well as three-dimensional volume data. From the statistical analysis, a better idea of the size distribution of NPs on or near the surface of the polymer is obtained. No significant faceting was observed and the assumption that the Au NPs are not exactly spherical in shape is valid. These Au NPs are oblate ellipsoids with the axis perpendicular to the surface being typically the shortest. The direct measurement of the mean thickness of NPs from the calibrated HAADF-STEM plan-view image renders more accurate data on the volume of Au NPs even if they are half buried in the polymer surface. The above method of formation of Au NPs by reduction of different reducing not only produced NPs on the surface but also below the surface inside the SU-8 polymer matrix. Au NPs formed by reduction using varying reducing agents differ in size according to the strength of reducing agent and range from 2 to 20 nm in diameter. The cross-sectional TEM micrograph in Figure 4(a) reveals that hydroquinone, being a bulky reducing agent, does not penetrate into the polymer matrix and the Au NPs are formed on the surface of the polymer. With $NaBH_4$ the Au NPs are much smaller 2–5 nm and are aligned in a band almost 10–20 nm below the polymer surface. SU-8 is used in fabrication of micro and nanoscale devices due to the small amount of shrinkage upon polymerization. The distribution of Au NPs should play an important role for the selective deposition of metal NPs for fabrication purposes.

Our technique measures the volume of Au NPs directly from the intensity-calibrated HAADF-STEM images rather than measuring the diameter. As a result, this technique reduces the experimental error in the measurement of the radius of the NP considerably. Statistical analysis identifies the dominant shape of the NPs when they are not exactly spherical. In this method the local background noise has been subtracted in the HAADF-STEM image for individual NPs to consider the small changes in height of the polymer layer beneath. For Au NPs, we show in Figure 3 that a thickness as high as 50 nm can be reliably determined from calibrated HAADF-STEM micrographs. Special care has to be taken that the NP is well focused to ensure that local thicknesses can be accurately determined from HAADF-STEM micrographs, especially at the NP edges where the thickness variation is large. However, if the integrated intensity is used to determine the volume of an NP small defocusing effects do not significantly change the calculated volume as HAADF-STEM uses mostly incoherently scattered electrons. Defocusing merely blurs the outline of an NP making it more difficult to define its edge. Our method of analysis of Au NPs can be extended to other systems where we find a distribution of NPs on the surface of a substrate.

Acknowledgements

This work was supported by NSF grant #0748712 and NSF-CHE grant #0809821. We acknowledge Triquint Semiconductors (Apopka, FL, U.S.A.) for providing us with multilayered samples and financial support. We also thank all the staff members of Advanced Material Processing and Analysis Center at the University of Central Florida (UCF) for providing support and help with handling of the instruments for the measurements. We acknowledge Dr. Florencio Eloy Hernández from Department of Chemistry at the UCF for providing gold standard NPs.

References

Aert, S.V., Verbeeck, J., Erni, R., Bals, S., Luysberg, M., Dycka, D.V. & Tendeloo, G.V. (2009) Quantitative atomic resolution mapping using high-angle annular dark field scanning transmission electron microscopy. *Ultramicroscopy* **109**(10), 1236–1244.

Anderson, R. (2002) Comparison of FIB TEM specimen preparation methods. *Proc. Microsc. Microanal.* **8**, 44–45.

Brostow, W., Gorman, B.P. & Olea-Mejia, O. (2007) Focused ion beam milling and scanning electron microscopy characterization of polymer + metal hybrids. *Mater. Lett.* **61**(6), 1333–1336.

Campo, A.D. & Greiner, G. (2007) SU-8: a photoresist for high-aspect-ratio and 3D submicron lithography. *J. Micromech. Microeng.* **17**, R81–R95.

Chen, Y., Tal, A., Kuebler, S. & Florida, C. (2007) Route to three-dimensional metallized microstructures using cross-linkable epoxide SU-8. *Chem. Mater.* **19**(16), 3858–3860.

Daniel, M.C. & Astruc, D. (2004) Gold nanoparticles: assembly, supramolecular chemistry, quantum-size-related properties, and applications toward biology, catalysis, and nanotechnology. *Chem. Rev.* **104**, 293–346.

Danscher, G. (1981) Histochemical demonstration of heavy metals: a revised version of the sulphide silver method suitable for both light and electronmicroscopy. *Histochemistry* **71**, 1–16.

DiScipio, R.G. (1996) Preparation of colloidal gold particles of various sizes using sodium borohydride and sodium cyanoborohydride. *Anal. Biochem.* **236**(1), 168–170.

Heinrich, H., Yuan, B., Nukala, H. & Yao, B. (2009) Quantitative scanning transmission electron microscopy for the measurement of thicknesses and volumes of individual nanoparticles. *Proc. Mater. Res. Soc.* **1184**, 119–124.

Huang, J. (2004) Combining Ar ion milling with FIB lift-out techniques to prepare high quality site-specific TEM samples. *J. Microsc.* **215**(3), 219–223.

James, E.M. & Browning, N.D. (1999) Practical aspects of atomic resolution imaging and analysis in STEM. *Ultramicroscopy* **78**, 125–139.

Khalid, M., Pala, I., Wasio, N. & Bandyopadhyay, K. (2009) Functionalized surface as template for in situ generation of two-dimensional metal nanoparticle assembly. *Colloids Surf. A Physicochem. Eng. Asp.* **348**(1–3), 263–269.

Knake, R., Fahmi, A., Tofail, S., Clohessy, J., Mihov, M. & Cunnane, V. (2005) Electrochemical nucleation of gold nanoparticles in a polymer film at a liquid-liquid interface. *Langmuir* **21**(3), 1001–1008.

Kübel, C., Voigt, A., Schoenmakers, R., Otten, M., Su, D., Lee, T.C., Carlsson, A. & Bradley, J. (2005) Recent advances in electron tomography: TEM and HAADF-STEM tomography for materials science and semiconductor applications. *Microsc. Microanal.* **11**(5), 378–400.

LeBeau, J.M., Findlay, S.D., Allen, L.J. & Stemmer, S. (2008a) Quantitative atomic resolution scanning transmission electron microscopy. *Phys. Rev. Lett.* **100**(20), 206101-04.

LeBeau, J.M., Findlay, S.D., Allen, L.J. & Stemmer, S. (2008b) Quantitative HAADF-STEM and EELS. *Microsc. Microanal.* **14**, 1352–1353.

LeBeau, J. M., Alfonso, A.J.D., Findlay, S.D., Stemmer, S. & Allen, L.J. (2009) Quantitative comparisons of contrast in experimental and simulated bright-field scanning transmission electron microscopy images. *Phys. Rev. B.* **80**(174106), 1–5.

Li, J., Malis, T. & Dionne, S. (2006) Recent advances in FIB–TEM specimen preparation techniques. *Materials Charact.* **57**(1), 64–70.

Loos, J., Duren, J.K.J.V & Morrissey, F. (2002) The use of the focused ion beam technique to prepare cross-sectional transmission electron microscopy specimen of polymer solar cells deposited on glass. *Polymer* **43**(26), 7493–7496.

Lockwood, D.J. (2007) *Functional Nanostructures, Processing, Characterization and Applications* (ed. by S. Seal), pp. 423–440. Springer, New York.

Mallory, G. & Hajdu, J. (1990) *Electroless Plating: Fundamentals and Applications*, pp. 441–461. Noyes/W. Andrew, New York.

McMahon, G., Rybczynski, J., Wang, Y., *et al.* (2009) Applications of multibeam SEM/FIB instrumentation in the integrated sciences. *Micros. Today* **17**(4), 34–39.

Menard, L.D, Gao, S.P., Xu, H., *et al.* (2006a) Sub-nanometer Au monolayer-protected clusters exhibiting molecule-like electronic behavior: quantitative high-angle annular dark-field scanning transmission electron microscopy and electrochemical characterization of clusters with precise atomic stoichiometry. *J. Phys. Chem. B* **110**(26), 12874–12883.

Menard, L.D., Xu, H., Gao, S.P., *et al.* (2006b) Metal core bonding motifs of monodisperse icosahedral Au13 and larger Au monolayer-protected clusters as revealed by X-ray absorption spectroscopy and transmission electron microscopy. *J. Phys. Chem. B* **110**(30), 14564–14573.

Nellist, P.D. & Pennycook, S.J. (1998) Accurate structure determination from image reconstruction in ADF STEM. *J. Microsc.* **190**(1/2), 159–170.

Patterson, J.R., Mayer, D., Weaver, L. & Phaneuf, M.W. (2002) FIB-TEM preparation for ex-situ cross-sectional and plan-view FIB specimen preparation. *Proc. Microsc. Microanal.* **8**(Suppl. 2), 566CD–567CD.

Prestridge, E.B., Via, G.H. & Sinfelt, J.H. (1977) Electron microscopy studies of metal clusters: Ru, Os, Ru–Cu, and Os–Cu. *J. Catal.* **50**(1), 115–123.

Reetz, M.T., Maase, M., Schilling, T. & Tesche, B. (2000) Computer image processing of transmission electron micrograph pictures as a fast and reliable tool to analyze the size of nanoparticles. *J. Phys. Chem. B* **104**, 8779–8781.

Sanders, J.V. (1986) Transmission electron microscopy of catalysts. *J. Electron Microsc. Tech.* **3**(1), 67–93.

Shankar, R., Shahi, V. & Sahoo, U. (2010) Comparative study of linear poly(alkylarylsilanes) as reducing agents toward Ag(I) and Pd(II) ions−synthesis of polymer−metal nanocomposites with variable size domains of metal nanoparticles. *Chem. Mater.* **22**(4), 1367–1375.

Taleb, A., Mangeney, C. & Ivanova, V. (2011) Metallic nanostructure formation using self assembled chemically anchored gold nanoparticles. *J. Electrochem. Soc.* **158**(2), K28–K34.

Troupis T, Triantis T, Hiskia A & Papaconstantinou, E. (2008) Rate-redox-controlled size selective synthesis of silver nanoparticles using polyoxometalates. *Eur. J.* Inorg. Chem. **36**, 5579–5586.

Williams, D.B. & Carter, C.B. (1996) *Transmission Electron Microscopy*, Vol **3**, pp. 358–367. Kluwer Academic/Plenum Publishers, New York.

Yan, Y., Rashad, M., Teo, E., Tanoto, H., Teng, J. & Bettiol, A. (2011) Selective electroless silver plating of three dimensional SU-8 microstructures on silicon for metamaterials applications. *Opt. Mater. Express* **1**(8), 1548–1554.

Yuan, B., Heinrich, H., Yao, B. & Dutta, A. (2010) Quantitative measurement of volumes for nanoparticles by high-angle annular dark-field scanning transmission electron microscopy. *Microsc. Microanal.* **16**(S2), 1764–1765.